Article

Not peer-reviewed version

An Adiabatic-Expansion-Induced Perturbation Study on Gas-Aerosol Partitioning in Ambient Air - Formation of NH4NO3 and Microdroplet Nitrogen Fixation (2)

Yating Gao , Qinchu Fan , Yujiao Zhu , Hengqing Shen , Qi Yuan , Yang Gao * , Huiwang Gao , Xiaohong Yao *

Posted Date: 28 March 2025

doi: 10.20944/preprints202503.2201.v1

Keywords: gas-aerosol partitioning; redox reaction; micro-droplet chemistry; atmospheric NH3; NH4NO3 aerosol

Article

An adiabatic-Expansion-Induced Perturbation Study on Gas-Aerosol Partitioning in Ambient Air - Formation of NH_4NO_3 and Microdroplet Nitrogen Fixation (2)

Yating Gao [1], Qinchu Fan [1], Yujiao Zhu [2], Hengqing Shen [2], Qi Yuan [1,3,4], Yang Gao [1,3,4,*], Huiwang Gao [1,3,4] and Xiaohong Yao [1,3,4,*]

[1] Key Laboratory of Marine Environment and Ecology (MoE), and Frontiers Science Center for Deep Ocean Multispheres and Earth System, Ministry of Education, Ocean University of China, Qingdao, 266100, China

[2] Environment Research Institute, Shandong University, Qingdao, 266327, China

[3] Sanya Oceanographic Institution, Ocean University of China, Sanya, 572024, China

[4] Laboratory for Marine Ecology and Environmental Science, Qingdao Marine Science and Technology Center, Qingdao, 266237, China

* Correspondence: yanggao@ouc.edu.cn (Y.G.); xhyao@ouc.edu.cn (X.Y.)

Abstract: Recent observations have increasingly challenged the conventional understanding of atmospheric NH_3 and its potential sources in remote environments. Laboratory studies suggest that microdroplet redox generation of NH_3 could offer an alternative explanation. However, key questions remain: 1) Can microdroplet redox generation of NH_3 occur in ambient air? 2) Is it restricted by the presence of specific catalysts? 3) What factors determine the efficiency of ambient NH_3 generation via microdroplet redox reactions? We investigate these questions based on adiabatic-expansion-induced perturbation observations performed in various atmospheres over the last decade. Our results indicate the adiabatic-expansion-induced generation of NH_3+HNO_3 at ultrafast formation rates, with campaign-dependent stable stoichiometric ratio of HNO_3 to NH_3, as well as highly variable occurrence frequencies and efficiencies. These findings suggest that microdroplet redox reactions are more likely responsible for the generation of NH_3+HNO_3 than conventional atmospheric NH_3 chemistry. Moreover, our analysis suggests that the line speed of microdroplets may be one of the key factors in determining the occurrence, stoichiometric ratio and efficiency of the redox reaction. Additionally, the presence of sea-salt aerosols and low ambient temperature, rather than the specific catalysts, may significantly influence these processes. However, the current observational data do not allow us to derive a functional relationship between the redox reaction rate and these parameters, nor to fully detail the underlying chemistry. Comprehensive and controlled laboratory experiments, similar to our adiabatic-expansion-induced observations but utilizing state-of-the-art highly sensitive analyzers, would be necessary, though such experiments are beyond our current capabilities.

Keywords: gas-aerosol partitioning; redox reaction; micro-droplet chemistry; atmospheric NH_3; NH_4NO_3 aerosol

1. Intruduction

Ammonia (NH_3) dominates the gas-phase alkaline species in the atmosphere and acts as the major contributor to neutralize atmospheric acids secondarily generated from natural and anthropogenic precursors [1–3]. Atmospheric NH_3 is widely recognized as being derived from various natural and anthropogenic sources in surface environments on the earth, including chemical fertilizers, livestock, natural soils and oceans, etc. [1,4–6]. However, satellite measurements have detected significant concentrations of NH_3 (above 15 pptv) in the upper troposphere and lower

 doi:10.20944/preprints202503.2201.v1

stratosphere (UTLS) over the subtropical regions of the southeastern Asian continent (20°-30°N, 70°-110°E) during the summer monsoon season, along with abundant neutralized NH_4NO_3 in the UTLS over remote oceanic zones, while the puzzle remains poorly understood [7–9]. In addition, whether oceans act as a net source or a net sink for NH_3 in remote, clean marine atmospheres is also a topic of ongoing debate [10–13]. Could these remote atmospheres harbor unrecognized sources of NH_3? This question, with its inherent complexity, may extend far beyond the conventional paradigm on NH_3 budgets in the atmosphere [14,15].

Excluding biogenic release of atmospheric NH_3, as well as the burning of fossil fuels and biomass, industrial NH_3 synthesis on Earth typically requires harsh operating conditions, such as high pressure, high temperature and highly efficient catalysts [1,5]. To circumvent these harsh conditions, there has been significant interest in the electrochemical reduction of NO and N_2 [15,16]. However, this process is severely restricted by the lack of efficient catalysts. Recently, Song et al. [14] reported a novel method for generating NH_3 under ambient conditions without the application of external electric potential or irradiation, i.e., spraying water microdroplets onto a magnetic iron oxide (Fe_3O_4) and Nafion-coated graphite mesh using compressed N_2 or air. The extremely strong perturbation signals of NH_4NO_3 reported in the companion paper raises two questions: 1) Does microdroplet-driven generation of NH_3 occur widely in cold, moist ambient air? and 2) Is the efficiency of microdroplet ammonia synthesis determined by the line speed of moving droplets, regardless of the presence of specific catalysts?

In this paper, we attempt to explore four key issues: 1) Whether the extremely strong perturbation signals of NH_4NO_3 resulted from the microdroplet redox generation reaction of NH_3 and HNO_3, followed by perturbation formation of NH_4NO_3? 2) Whether the microdroplet redox reaction of NH_3 and HNO_3 is independent of catalysts? 3) Whether the line speed of moving droplets determines the probability for occurring redox reactions of NH_3 and HNO_3, or the oxidation reactions of HNO_3 alone or organic nitrate? 4) What future studies are needed for microdroplet ammonia synthesis and the development of a new paradigm for atmospheric NH_3, particularly in marine atmospheres abundant in fast-moving microdroplets?

2. Experimental

This study includes data collected from coastal and marine atmospheres during nine distinct campaigns. Campaigns 1–7 were defined identically to those in the companion paper, i.e., four coastal campaigns performed in Qingdao, China, during the heating seasons in 2013, 2015 and 2022 (Campaigns 2 - 4), as well as the non-heating season in 2013 (Campaign 1), and three marine campaigns as Campaigns 5-7 over the marginal seas of China in November - December 2012, 2013 and July- August 2016 [17], respectively. Campaign 8 was performed at a coastal site <1 km away from that used for Campaign 4, with nine sets of samples collected during the summer of 2019 on 11, 20, 21 July, and 1, 4, 5, 6, 12 and 13 August. The chemical analysis was consistent with those detailed in Yu et al. [18], Xie et al. [19] and Hu et al. [20]. In addition, some Nano-MOUDI results from the spring and summer marine campaigns of 2015, as reported by Yu et al. [18], were also referenced for discussion. Campaign 9 was performed over the South China Sea (SCS, a tropical region) from 29 March to 2 May 2017 [21]. Eleven sets of Nano-MOUDI samples were collected during the campaign, with two sets intentionally gathered on 15 and 18 April to capture strong self-vessel combustion emissions. The remaining samples were collected on 30 March (en route to the South China Sea from the anchor port), 2, 7, 11, 21, 22, 23, 26, and 29 April. Note that 0.5%-1.0% high sulfur-content diesel was commonly used on research vessels at that time in China.

An Ambient Ion Monitor−Ion Chromatograph (AIM-IC, URG-9000D) was used for simultaneous sampling during Campaign 3 and part of Campaign 4, but not in the other campaigns. Moreover, the E-AIM model was employed to calculate the gas-aerosol partitioning of semi-volatile species [22] (http://www.aim.env.uea.ac.uk/aim/aim.php, last access: 20 January, 2025). For the cruise campaigns, meteorological data were obtained from an automatic meteorological station on the vessel. For the coastal campaigns, the meteorological data were download from the meteorological

 doi:10.20944/preprints202503.2201.v1

data were download from China Meteorological Data Service Centre (https://data.cma.cn/, last access: 25 January, 2025).

3. Materials and Methods

3.1. Perturbation Formation of Comparable NH_4NO_3 and Organic Nitrate in Campaigns 8 and 9

In Campaign 8, the strongest perturbation formation of NH_4NO_3 was detected at the size bin of 0.032-0.056 μm on 20 July 2019 (Figures 1a, b). The existence of higher NH_4NO_3 concentrations in atmospheric particles within the 0.032-0.056 μm size range, compared to the 0.056-0.10 μm size range with an identical $dlogD_p$ value, was theoretically and practically impossible due to the size-dependent Kelvin effect and the universally observed larger surface area of atmospheric particles in the latter size range [3,23]. The Kelvin effect has also been reported to result in higher SO_4^{2-} concentrations than NO_3^- in atmospheric particles smaller than 100 nm [24], and did not support that over one order of magnitude higher concentration of NO_3^- (23 neq m^{-3}) than that of SO_4^{2-} (0.47 neq m^{-3}) observed at 0.032-0.056 μm size range (Figure 1a, c). Even surprisingly, the detected molar concentration of NH_4^+ at that size bin was only accounted for approximately 1/4 of the corresponding NO_3^- concentration. This raised the possibility of perturbation formation of organic nitrate, which was commonly detected in ambient air [25,26], to account for the NO_3^- unexplained by NH_4^+. Organic nitrate might have dissolved into the deionized water and been detected by the ion chromatography as NO_3^-. On the same day, strong perturbation formation of MSA^- was also detected, but not for SO_4^{2-} and $DMAH^+$. On the remaining days of Campaign 8, substantially weak perturbation formation of particulate nitrate was mostly observed at the 0.018-0.032 μm size bin. Again, the detected amount of NH_4^+ via perturbation formation was insufficient to explain the corresponding NO_3^- values.

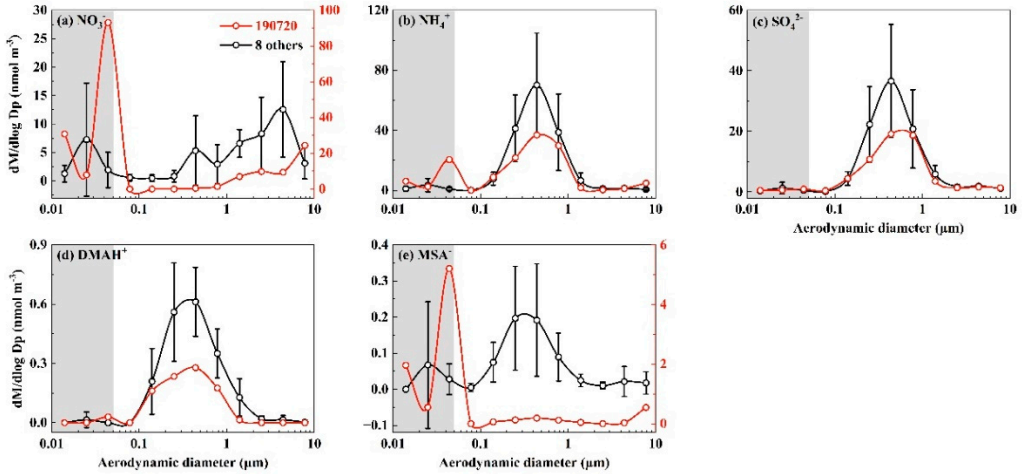

Figure 1. Molar concentration size distributions of five ions in atmospheric particles collected at a coastal site of Qingdao in 2019. (The data on 20 July was highlighted in red; the data on 11 and 21 July, and 1, 4, 5, 6, 12, 13 August were averaged and marked in black; the error bars represented the standard deviation in different samples).

In Campaign 9, the strongest perturbation formation of NH_4NO_3 was detected at the 0.032-0.056 μm size bin on 21 April 2017 (Figure 2a, b). However, similar to Campaign 8, the detected amount of NH_4^+ (2.9 neq m^{-3}) in this size range accounted for only about 1/5 of the corresponding NO_3^- value (15.5 neq m^{-3}). This suggested that approximately 80% of the detected NO_3^- might have existed as organic nitrate. The same can be said to the perturbation formation of organic nitrate on 15 and 18 April when the self-vessel combustion plumes were deliberately observed. However, the perturbation signals were substantially weaker on these two days than those on 21 April. On the remaining days, the perturbation signals for NO_3^- were generally too weak to confirm, and the same

 doi:10.20944/preprints202503.2201.v1

was true for SO_4^{2-} and $DMAH^+$. The lower occurrence frequency of perturbation formation of NH_4NO_3 and insufficient amount of NH_3 formed could be related to the reduced line speeds of air streams, as discussed in Section 3.4.

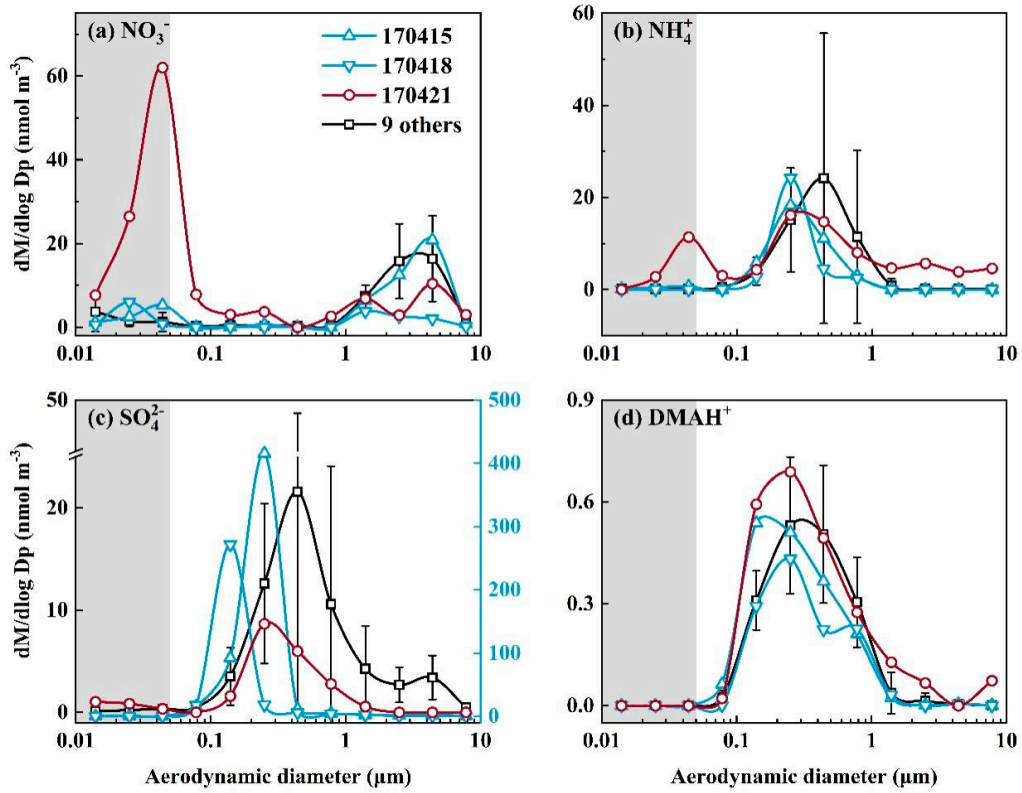

Figure 2. Molar concentration size distributions of four ions in atmospheric particles collected over the South China Sea in 2017 (The data on 21 April was highlighted in red; the data on 15 and 18 April were featured by largely increased concentrations of SO_4^{2-} derived from self-vessel combustion and were highlighted in blue; the data on 30 March, 2, 7, 11, 21, 22, 23, 26, 29 April were averaged and marked in black; the error bars represented the standard deviation in different samples).

3.2. Whether Is Adiabatic Perturbation Alone Sufficient to Explain NO_3^- and NH_4^+ Detected on the Last Three Stages of Nano-MOUDI Sampling in Cold Coastal Atmospheres?

To determine whether enhanced gas-aerosol partitioning alone is sufficient to generate the perturbation amount of NH_4NO_3 in the last three stages of Nano-MOUDI sampling in coastal atmospheres, additional simultaneous measurements of HNO_3 and NH_3 gases, along with their counterparts in $PM_{2.5}$, are required. Therefore, the perturbation formation of NH_4NO_3 during Campaign 3 were selected to examine the hypothesis (Figure 3). To increase the dataset for correlation analysis, two samples collected over the Yellow Sea and the Bohai Sea, taken two and a half months prior to Campaign 3, were also included, as their perturbation characteristics were more similar to those observed in Campaign 3 rather than in other marine campaigns. Strong perturbation formation of particulate NO_3^- was observed in 5 of 11 samples, with NO_3^- concentrations in $PM_{0.010\text{-}0.056}$ exceeding those in $PM_{0.056\text{-}1.0}$ by more than double (Figures 3a, b). The perturbation was, however, negligible in 2 out of 11 samples, with the remaining samples falling between these two extremes.

 doi:10.20944/preprints202503.2201.v1

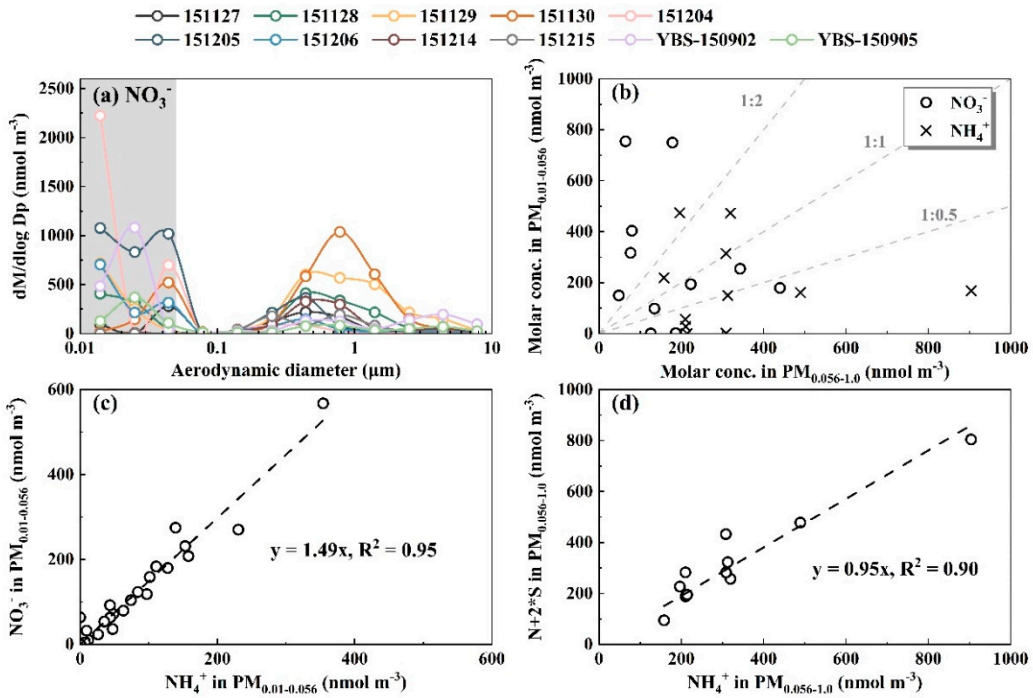

Figure 3. Molar concentration size distributions of NO_3^- (a), and correlations between different variables for NO_3^- and NH_4^+ in $PM_{0.010\text{-}0.056}$ vs. the corresponding values in $PM_{0.056\text{-}1.0}$ (b), NO_3^- vs. NH_4^+ in different sized $PM_{0..010\text{-}0.056}$ (c), and N+2*S vs. NH_4^+ in $PM_{0.056\text{-}1.0}$ (d) during Campaign 3. The letters N and S in (d) represent concentrations of NO_3^- and SO_4^{2-}, respectively (YBS-150902 and YBS-150905 samples were collected in marine atmospheres over the Yellow Sea and Bohai Sea during a cruise campaign in September 2015).

As shown in Figure 4 and analyzed in detail below, the perturbation caused by the thermodynamic equilibrium shift alone cannot explain most of higher concentrations of NO_3^- in $PM_{0.010\text{-}0.056}$ than the corresponding values in $PM_{2.5}$, as well as some of NH_4^+ with higher concentrations in $PM_{0.010\text{-}0.056}$. When gas-aerosol thermodynamic equilibrium analyses were conducted using the particulate concentrations of chemical species measured by the AIM-IC in $PM_{2.5}$ and by the Nano-MOUDI in $PM_{0.010\text{-}3.2}$, respectively, along with gaseous species measured by the AIM-IC, the modeled results indicated that the gas-aerosol equilibrium was reasonably achieved (Figures 4a, b, d, e). The slightly over-predicted equilibrium concentrations of NO_3^- and under-predicted NH_4^+ in $PM_{2.5}$, might be attributed to the exclusion of NH_4Cl and ammonium organics in $PM_{2.5}$ from the modeling. This argument was supported by the consistent equilibrium concentrations of NO_3^- and NH_4^+ in $PM_{0.010\text{-}3.2}$ with the corresponding observed values, which were significantly higher than those in $PM_{2.5}$. This increase likely reduced the impact of the exclusion on the modeled equilibrium concentrations.

With the gas-aerosol thermodynamic equilibria to be achieved, adiabatic-expansion-induced perturbation would cause a shift in the equilibrium, leading to additional gaseous NH_3 and HNO_3 partitioning into the particle phase (Figure 4c, f). This was clearly demonstrated in Figure 4c, where the concentrations of (NH_{3gas} + NH_4^+ in $PM_{2.5}$) measured by the AIM-IC were plotted against the corresponding NH_4^+ in $PM_{0.010\text{-}3.2}$, with four data points aligning along the 1:1 line. On 14 and 15 December, 2015, two data points aligned with the 1:1 line when the concentrations of (HNO_{3gas} + NO_3^- in $PM_{2.5}$) measured by the AIM-IC were plotted against the corresponding NO_3^- in $PM_{0.010\text{-}3.2}$. On these two days, the data points in Figure 4c slightly scattered above the 1:1 line. However, 7 out of 9 data points in Figure 4f and 2 out of 9 data points in Figure 4c scattered far below the 1:1 line. In these cases, additional ultrafast oxidation and/or redox reactions definitely occurred, resulting in the formation of (HNO_3+NH_3) and organic nitrate in the last three-stage sampling.

 doi:10.20944/preprints202503.2201.v1

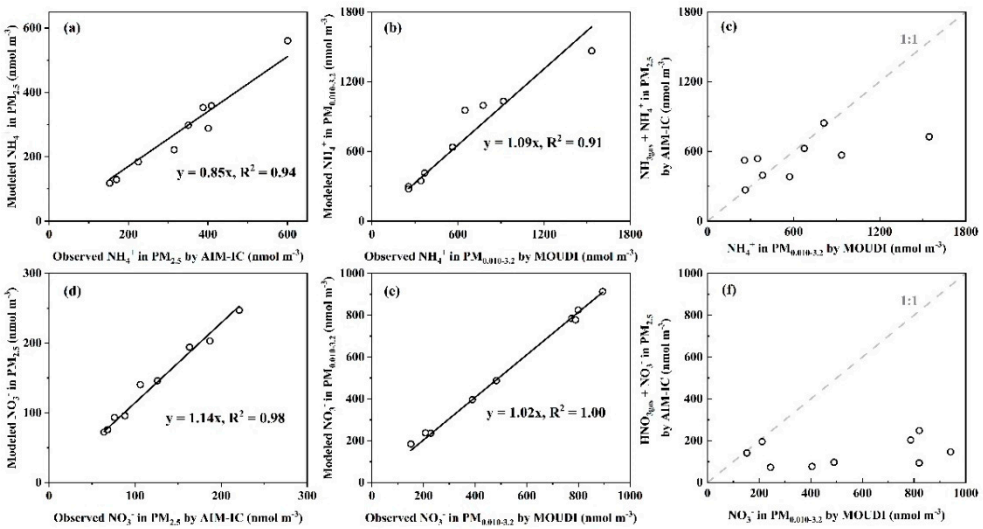

Figure 4. Correlations between modeled NH_4^+ vs. observed NH_4^+ in $PM_{2.5}$ collected by AIM-IC (a), modeled NH_4^+ vs. observed NH_4^+ in $PM_{0.010\text{-}3.2}$ collected by MOUDI (b), (NH_{3gas} + NH_4^+ in $PM_{2.5}$) measured by the AIM-IC vs. the corresponding NH_4^+ in $PM_{0.010\text{-}3.2}$ measured by MOUDI (c), modeled NO_3^- vs. observed NO_3^- in $PM_{2.5}$ collected by AIM-IC (d), modeled NO_3^- vs. observed NO_3^- in $PM_{0.010\text{-}3.2}$ collected by MOUDI (e), (HNO_{3gas} + NO_3^- in $PM_{2.5}$) measured by the AIM-IC vs. the corresponding NO_3^- in $PM_{0.010\text{-}3.2}$ measured by MOUDI (f).

Based on the size distributions presented in Figure 3a, the maximum NO_3^- concentration via perturbation formation occurred across various size bins. By considering the sampling flow, the diameters (~200 μm) and numbers of nozzles (2940), the maximum line speed of air streams passing through the last three-stage nozzles can be roughly estimated to ~$5*10^2$ m s^{-1}. Giving this estimation, the observed perturbation formation of NO_3^- must have occurred at an ultrafast rate, within approximately $1*10^{-4}$ s. However, the line speed of air streams should largely decrease after they left the nozzle outlet. The ultrafast redox and oxidation reactions of NH_3, HNO_3 and organic nitrate differ from those traditionally recognized reactions in atmospheric chemistry included in various air quality or climate modeling [3]. These reactions likely occurred via microdroplet chemistry when the microdroplets were sprayed at an ultrafast moving-speed [14,27,28]. While the contribution of vacuum ionization cannot be entirely ruled out [29], it is likely a minor factor due to the incomplete vacuum condition in the last three stages of MOUDI (~0.4 atm). In addition, NO, one of the gaseous pollutants primarily emitted from vehicle exhaust, industrial plants, or thermal power stations, can be converted to NH_3 using three-way catalysts equipped on vehicles [30]. The simultaneously observed concentrations of NO and NO_2, as shown in Figure S1, could be sufficient to generate NH_3, HNO_3 and organic nitrate via microdroplet chemistry, however, we did not measure microdroplets directly. Moreover, there were no significant correlations between the average ambient temperature or relative humidity and the perturbation-formed particulate nitrate (Figure S1). Note that the theory on spontaneous microdroplet redox chemistry has only recently become available [31]. Therefore, it is unsurprising that the unexpectedly high concentrations of NO_3^- and NH_4^+ observed at the last three stages cannot be timely explained.

When the concentrations of NO_3^- in the 0.010-0.056 μm size bins were plotted against the corresponding NH_4^+ values (Figure 3c), a good correlation was obtained, with a slope of 1.49. This slope also suggested that 1/3 of the observed NO_3^- via perturbation formation likely existed as organic nitrate. However, the ratio of N+2*S to NH_4^+ in $PM_{0.056\text{-}1.0}$ was 0.95 (Figure 3d), implying that NO_3^- and SO_4^{2-} in this size range were primarily associated with NH_4^+ and were almost completely neutralized.

In addition, some samples exhibited a distinct droplet mode of NO_3^- at 1-2 μm (Figure S2), conventionally attributed to fog-processing of aerosols [3]. This unique feature suggests the possibility that the microdroplet chemistry may have occurred in larger size bins for some samples of the Campaign 3. Based on the observational data, we artificially assumed that the microdroplet

 doi:10.20944/preprints202503.2201.v1

chemistry could cause 100% of the positive artifacts in the first four samples collected on 27-30 November, 2015. Under this assumption, we surprisingly gained the new good correlations as follows (Figure S3): $[NH_4^+]_{PM2.5} = 0.92 * [NH_4^{+*}]_{PM0.056-3.2}$, R^2=0.94, P<0.01; $[SO_4^{2-}]_{PM2.5} = 1.02 * [SO_4^{2-*}]_{PM0.056-3.2}$, R^2=0.97, P<0.01; $[NO_3^-]_{PM2.5} = 0.69 * [NO_3^{-*}]_{PM0.056-3.2}$, R^2=0.98, P<0.01. The tested results, however, require further validation in future studies.

3.3. Adiabatic Perturbation Superimposed Ultrafast Formation of Huge Amounts of NH_4NO_3 and Organic Nitrate at the Last Three Stages of Nano-MOUDI Sampling in Marine Atmospheres

In Campaign 5, strong perturbation formation of NH_4NO_3 was observed in 4 out of 14 samples (Figures 5a, b, c). The maximum perturbations occurred at size range of 0.032-0.056 μm and 0.018-0.032 μm, respectively. A strong correlation with a unity slope was found when the concentrations of NO_3^- in $PM_{0.010-0.056}$ were plotted against corresponding NH_4^+ concentrations, indicating no detectable perturbation formation of organic nitrate. Although simultaneous measurements of NH_{3gas} and HNO_{3gas} were not available during this period, our observations from the marine atmosphere in April 2018 and December 2019 suggested that the adiabatic perturbation alone cannot account for the observed NH_4NO_3 formation. Alternatively, ultrafast redox reactions of NH_3 and HNO_3 were required. During the 2012 cruise campaign, SO_4^{2-} and NO_3^- in $PM_{0.056-1.0}$ appeared to be completely neutralized by NH_4^+ (Figure 5d).

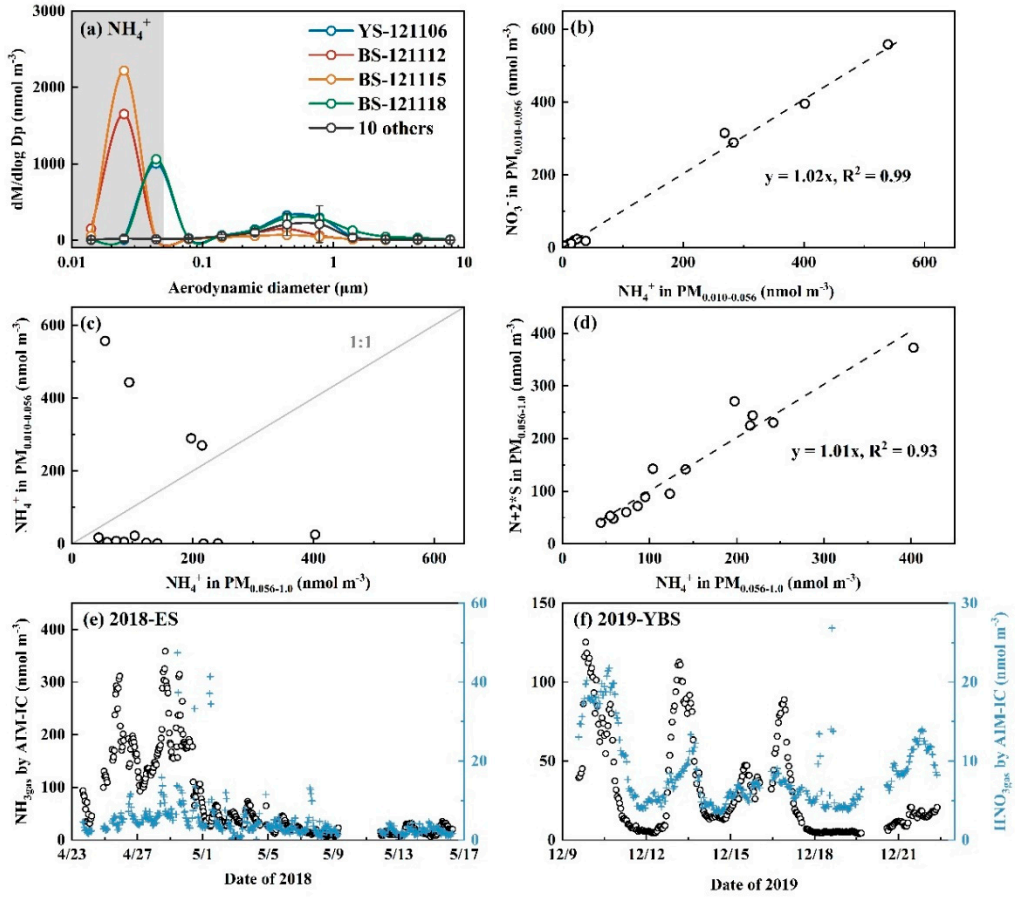

Figure 5. Molar concentration size distributions of NH_4^+ (a), NO_3^- vs. NH_4^+ in $PM_{0.010-0.056}$ (b), NH_4^+ in $PM_{0.010-0.056}$ vs. that in $PM_{0.056-1.0}$ (c), N+2*S vs. NH_4^+ in $PM_{0.056-1.0}$ (d) during Campaign 5; time series of NH_{3gas} and HNO_{3gas} in the marine atmosphere over the East China Sea (ES) measured by the AIM-IC in April 2018 [12] (e), same as (e) but over the Yellow Sea and Bohai Sea (YBS) in December 2019 [32]. The letters N and S in (b) represent concentrations of NO_3^- and SO_4^{2-}, respectively.

 doi:10.20944/preprints202503.2201.v1

Even stronger perturbation formation of NH_4NO_3 occurred during Campaign 6 (Figures 6a, b, c). Again, no detectable organic nitrate was found concurrently with the perturbation formation of NH_4NO_3 (Figure 6d). It is interesting that the perturbation formation of NH_4NO_3 was negligible on the first two days (6-7 November, 2013) but intensified in the following days, with the maximum perturbation occurring at size bins varying a lot. In 8 out of 15 samples in Campaign 6, the perturbation formation of $NH_4NO_3 \geq 140$ μg m^{-3} (with NO_3^- reaching 202±71 μg m^{-3} and NH_4^+ at 61±4 μg m^{-3}). The substantial amount of NH_4NO_3 and ~10^{-4} s residence time of air streams definitely required ultrafast redox reactions of NH_3 and HNO_3 during sampling. It also indicated that such ultrafast redox reactions of NH_3 practically occurred under mild conditions without the need for additional electricity consumption. Unlike in Campaign 5, SO_4^{2-} and NO_3^- in $PM_{0.056\text{-}1.0}$ were likely incompletely neutralized by NH_4^+ in Campaign 6 (Figure 6e).

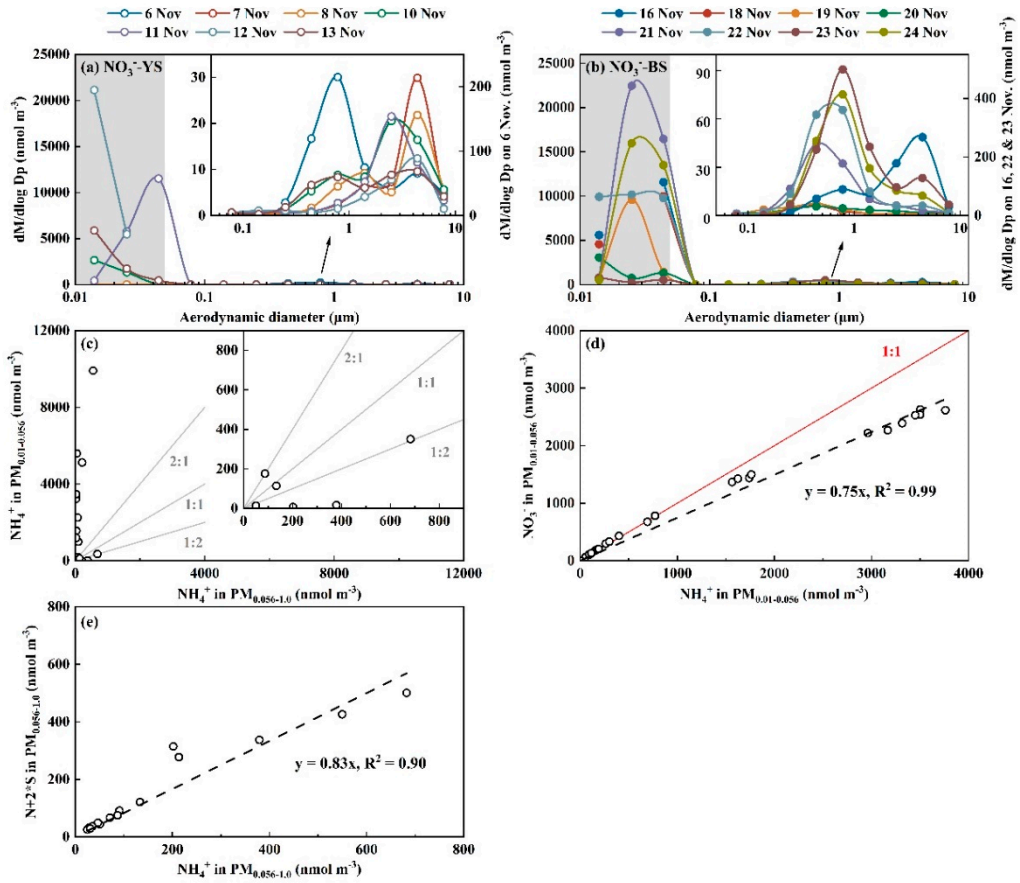

Figure 6. Molar concentration size distributions of NO_3^- on 6-13 November 2013 (a), those on 16-24 November 2013 (b), NH_4^+ in $PM_{0.010\text{-}0.056}$ vs. that in $PM_{0.056\text{-}1.0}$ (c), NO_3^- in $PM_{0.010\text{-}0.056}$ vs. NH_4^+ in $PM_{0.010\text{-}0.056}$ (d), N+2*S vs. NH_4^+ in $PM_{0.056\text{-}1.0}$ (e) during Campaign 6. The letters N and S in (e) represent concentrations of NO_3^- and SO_4^{2-}, respectively.

3.4. Key Factors in Determining Ultrafast Formation of (HNO_3+NH_3) and Organic Nitrate: Evidences and Uncertainties

To comply with the Second Law of thermodynamics, the ultrafast formation of (HNO_3+NH_3) and organic nitrate must be driven either by catalytic reactions or by the highly efficient conversion of energy from microdroplet motion into the electrochemical energy required. To investigate the occurrence of catalytic reactions, we compared the chemical comparisons between the 8th-stage and 12th-stage micro-orifice nozzle plates. The internal and external surface chemical compositions of the 8th-stage (S8) and 12th-stage (S12) plates, corresponding to the size bins of 0.18-0.32 μm and 0.018-0.032 μm, respectively, are shown in Figure 7. Both plates were primarily composed of aluminum

 doi:10.20944/preprints202503.2201.v1

and oxygen, which together accounted for 61%-76% of the total weight on internal and external surfaces, following by sulfur contributing 5.8%±0.7% of the total weight. No significant differences in these major components were detected between the internal and external surfaces of each plates. However, more Fe and Ni were detected on 12th-stage plates, accounting for 6.2% and 3.0% of the total weight, respectively. The role of these minor components as potential catalysts needs further investigation. However, potential catalytic reactions cannot explain the ultrafast formation of (HNO_3+NH_3) and organic nitrate being overwhelmed in a certain stage, e.g., Fig 4a and Fig 5b.

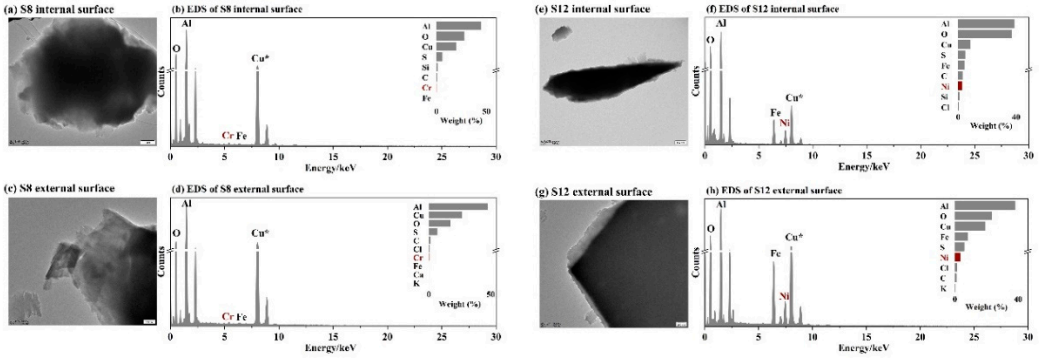

Figure 7. Morphology and main chemical composition of micro-orifice nozzle plates at S8 and S12: TEM image of internal surface of S8 (a), EDS spectrum of internal surface of S8 (b); The same as (a, b) but of external surface of S8 (c, d), of internal surface of S12 (e, f), and of external surface of S12 (g, h). Asterisk represents that Cu was excluded from the EDS spectrum because of the copper material of TEM grids.

Considering the conversion of energy from microdroplet motion into the electrochemical energy required for microdroplet chemistry, the high line speed of microdroplets might increase the microdroplet surface electric voltage and subsequently enhance ultrafast reactions [33]. Various perturbation levels of NO_3^- in $PM_{0.010-0.056}$ under different MOUDI sampling flow rates were thus analyzed in Figure 8. The perturbation levels are thoroughly defined in the companion paper [17], i.e., negligible and unconfirmable perturbation formation for levels 0-1, moderate perturbation formation for level 2, strong and extremely strong perturbation formation for levels 3-4. The efficiency of (HNO_3+NH_3) and organic nitrate generation expectedly increased with increasing air stream line speed through the nozzles. Additionally, sea salt aerosols and lower ambient temperature may further enhance the ultrafast reactions, as presented below.

1) The efficiency of NH_4NO_3 perturbation generation via microdroplet chemistry was found to be dependent on the air stream line speed through the nozzles, which was determined by the MOUDI sampling flow rate (Figures 7 and S4). For example, strong to extremely strong perturbation generation was observed during the 2015 coastal campaign and the 2012 and 2013 marine campaigns at a MOUDI (Model 122) flow rate of 29.4 L min^{-1}, corresponding to an air stream nozzle-outlet line speed of at least $5*10^2$ m s^{-1}. In contrast, no microdroplet chemistry was detected at a sampling flow rate of 10 L min^{-1} (using a different MOUDI, Model 125) during the November 2013 coastal campaign. However, the perturbation generation of organic nitrate was likely less influenced by the air stream line speed, as indicated by the presence of NO_3^- perturbation generation during the 2019 coastal campaign.

2) The presence of ultrafine sea salt aerosol significantly enhanced the efficiency of perturbation generation for (HNO_3+NH_3) and organic nitrate. As illustrated in Figure 8, the frequency of NO_3^- perturbation generation was higher in marine atmospheres than in coastal atmospheres. Specifically, 29 out of 60 samples collected from marine atmospheres were classified in Levels 2-4, whereas only 11 out of 64 samples from coastal atmospheres reached these levels. Additionally, the intensity of perturbation was greater in marine atmospheres, with 12 out of 15 samples falling into Levels 3-4 during the 2013 marine campaign, compared to only 3 out of 9 samples during the 2015 coastal campaign.

 doi:10.20944/preprints202503.2201.v1

3) Higher ambient temperature likely disfavored the perturbation generation of (HNO_3+NH_3) and organic nitrate, as evidenced by the absence of NH_4NO_3 perturbation generation during the May 2013 coastal campaign and the July 2016 marine campaign. However, it was also possible that higher ambient temperatures disfavored gas-aerosol partitioning. In such cases, the microdroplet-generated (HNO_3+NH_3) and organic nitrate gases may have passed directly through the nozzles rather than being captured on the filters.

Overall, an innovative and controllable experiment system is necessary to examine the uncertainties. For example, to study the impact of air stream line speed on the efficiency of perturbation generation for (HNO_3+NH_3) and organic nitrate, water microdroplet could be sprayed into a NO_2/N_2-filled (or NO/NO_2/N_2-filled) chamber through a nozzle at varying air stream line speeds, with temperature and pressure controlled. Ionic concentrations would be dynamically monitored to observe changes. Additionally, spraying NaCl-containing microdroplet and adjusting the system's temperature would enable further investigation into the effects of sea salt aerosol and ambient temperature on the efficiency of perturbation generation. Although our current experiments lacked the high temporal resolution to detect dynamic changes in microdroplets, this limitation may not pose a significant issue for the broader research community.

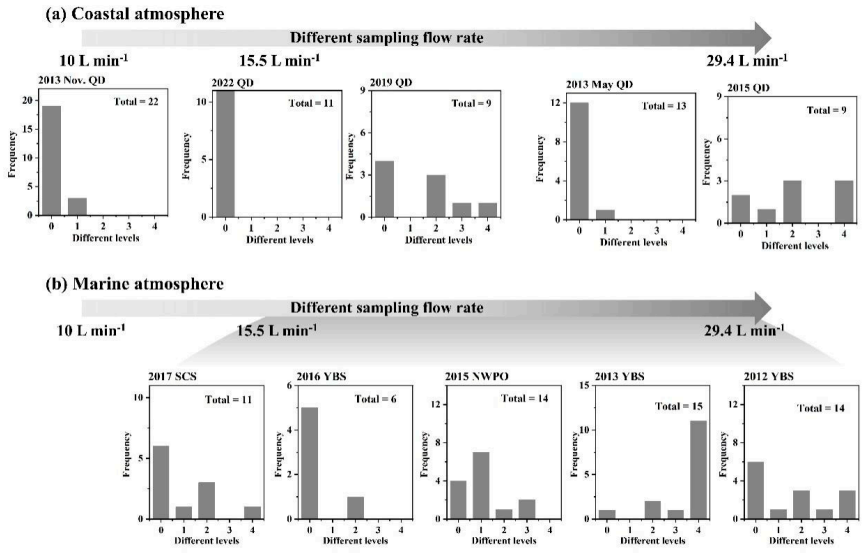

Figure 8. Different levels of NO_3^- perturbation formation in size bins 0.010-0.056 μm in coastal atmospheres (a) and marine atmosphere (b).

4. Implication

This study reports unique findings on the ultrafast redox reactions of generating substantial amounts of (HNO_3+NH_3) or organic nitrate in adiabatic-expanded ambient air within a time scale of approximately 10^{-4} s. Such ultrafast and highly efficient redox reactions of (HNO_3+NH_3) or organic nitrate have definitely not been previously recognized in the atmospheric chemistry community, and are not currently included in air quality and climate models. However, these reactions may occur due to microdroplet chemistry under ultrafast moving speeds of microdroplets.

There remain numerous uncertainties regarding these new findings, including: 1) Does low ambient temperature enhance the redox reaction of (HNO_3+NH_3) or organic nitrate? 2) What factors control the ratio of (HNO_3+NH_3) to organic nitrate in the ultrafast redox reactions in addition to line speeds of micro-droplets? 3) To what extent does sea salt aerosol significantly increase the efficiencies of redox reactions via microdroplet generation? 4) Does NH_3 generation occur from N_2 or NO? 5) Is this process critical for marine nitrogen cycling, particularly giving the presence of microdroplets during typhoon periods or strong cumulus convection? This may also apply to upper atmosphere. 6)

 doi:10.20944/preprints202503.2201.v1

Is the NH_3 emitted from on-road vehicles generated by ultrafast-moving microdroplets? 7) Does microdroplet chemistry influence the formation of secondary species in freshly emitted combustion plumes within the initial seconds?

Supplementary Materials: The following supporting information can be downloaded at the website of this paper posted on Preprints.org, Figure S1: Daily average of gases molar concentrations for SO_2, O_3, NO, NO_2 (a), and of temperature and relative humidity (b) in 2015; Figure S2: Molar concentration size distributions for NO_3^- on 28, 29, and 30 November, 2015. The green, orange, and red shaded areas represent the droplet mode fitted by a normal distribution in the size distributions of these three samples; Figure S3: Correlations between ionic concentrations in $PM_{2.5}$ measured by AIM-IC and those in $PM_{0.056\text{-}3.2}$ measured by MOUDI for NH_4^+ (a), SO_4^{2-} (b), and NO_3^- (c) in the samples collected on 27, 28, 29, and 30 November, 2015. NH_4^+*, SO_4^{2-}*, and NO_3^-* in (a-c) represent the corrected concentrations considering the 100% of the positive artifacts of these four samples in MOUDI sampling; Figure S4: Different levels of NH_4^+ perturbation formation in size bins 0.010-0.056 μm in coastal atmospheres (a) and marine atmosphere (b).

Author Contributions: Conceptualization, X.Y.; methodology, Y.G. (Yating Gao), Q.F., H.S. and Q.Y.; validation, X.Y. and Y.G. (Yating Gao); data curation, X.Y. and Y.G. (Yating Gao); writing—original draft preparation, Y.G. (Yating Gao); writing—review and editing, Q.F; Y.Z.; H.S.; Q.Y.; Y.G. (Yang Gao); H.G.; X.Y., ; supervision, X.Y.; funding acquisition, X.Y. All authors have read and agreed to the published version of the manuscript.

Funding: This research was funded by the Natural Science Foundation of China, grant number 42276036 and the Hainan Provincial Natural Science Foundation of China, grant number 422MS098.

Institutional Review Board Statement: Not applicable.

Informed Consent Statement: Not applicable.

Data Availability Statement: The original data presented in the study are openly available at https://data.mendeley.com and should be cited as follows: Gao, Yating; Fan, Qinchu; Zhu, Yujiao; Shen, Hengqing; Yuan, Qi; Gao, Yang; Gao, Huiwang; Yao, Xiaohong (2025), "Nano MOUDI-II sampling data from Qingdao and China's marginal seas in 2012-2022 (2)", Mendeley Data, V1, doi: 10.17632/96wn552btc.1.

Acknowledgments: This work was supported by the Natural Science Foundation of China (grant no. 42276036) and the Hainan Provincial Natural Science Foundation of China (grant no. 422MS098).

Conflicts of Interest: The authors declare no conflicts of interest.

Abbreviations

The following abbreviations are used in this manuscript:

AIM-IC	Ambient Ion Monitor – Ion Chromatograph
$DMAH^+$	particulate dimethylaminium
EDS	Energy Dispersive Spectrometer
ES	the East China Sea
E-AIM	Extended AIM Aerosol Thermodynamics Model
MSA^-	particulate methanesulfonic acid
Nano MOUDI-II	Nano Micro-Orifice Uniform-Deposit Impactor, second generation
N + 2 * S	the sum of the molar concentration of nitrate and twice the molar concentration of sulfate
$PM_{2.5}$	particulate matter with the aerodynamic diameter below 2.5 μm collected by AIM-IC
$PM_{0.010\text{-}0.056}$/$PM_{0.010\text{-}3.2}$/$PM_{0.056\text{-}1.0}$/$PM_{0.056\text{-}3.2}$	particulate matter with the aerodynamic diameter of 0.010-0.056/0.010-3.2/0.056-1.0/0.056-3.2 μm collected by Nano MOUDI-II
SCS	the South China Seat
S8/S12	the 8th or 12th stage of Nano MOUDI-II
TEM	Transmission Electron Microscope
UTLS	upper troposphere and lower stratosphere
YBS	the Yellow Sea and the Bohai Sea

 doi:10.20944/preprints202503.2201.v1

References

1. Behera, S.N.; Sharma, M.; Aneja, V.P.; Balasubramanian, R. Ammonia in the atmosphere: a review on emission sources, atmospheric chemistry and deposition on terrestrial bodies. *Environ Sci Pollut R* **2013**, *20*, 8092-8131.
2. Peng, J.; Hu, M.; Shang, D.; Wu, Z.; Du, Z.; Tan, T.; Wang, Y.; Zhang, F.; Zhang, R. Explosive secondary aerosol formation during severe haze in the North China Plain. *Environ Sci Technol* **2021**, *55*, 2189-2207.
3. Seinfeld, J.H.; Pandis, S.N. *Atmospheric Chemistry and Physics: From Air Pollution to Climate Change*, 3rd ed.; John Wiley & Sons, Inc.: New Jersey, 2016.
4. Altieri, K.E.; Fawcett, S.E.; Hastings, M.G. Reactive nitrogen cycling in the atmosphere and ocean. *Annu. Rev. Earth Planet. Sci.*, **2021**, *49*, 523-550.
5. Lan, Z.; Lin, W.; Zhao, G. Sources, Variations, and effects on air quality of atmospheric ammonia. *Curr Pollut Rep* **2024**, *10*, 40-53.
6. Nair, A.A.; Yu, F. Quantification of atmospheric ammonia concentrations: a review of its measurement and modeling. *Atmosphere* **2020**, *11*, 1092.
7. Froyd, K.D.; Murphy, D.M.; Sanford, T.J.; Thomson, D.S.; Wilson, J.C.; Pfister, L.; Lait, L. Aerosol composition of the tropical upper troposphere. *Atmos Chem Phys* **2009**, *9*, 4363-4385.
8. Ge, C.; Zhu, C.; Francisco, J.S.; Zeng, X.C.; Wang, J. A molecular perspective for global modeling of upper atmospheric NH3 from freezing clouds. *Proc. Natl. Acad. Sci.* **2018**, *115*, 6147-6152.
9. Höpfner, M.; Volkamer, R.; Grabowski, U.; Grutter, M.; Orphal, J.; Stiller, G.; von Clarmann, T.; Wetzel, G. First detection of ammonia (NH3) in the Asian summer monsoon upper troposphere. *Atmos Chem Phys* **2016**, *16*, 14357-14369.
10. Altieri, K.E.; Spence, K.A.M.; Smith, S. Air-sea ammonia fluxes calculated from high-resolution summertime observations across the Atlantic Southern Ocean. *Geophys Res Lett* **2021**, *48*, e2020GL091963.
11. Bouwman, A.F.; Lee, D.S.; Asman, W.A.H.; Dentener, F.J.; Van Der Hoek, K.W.; Olivier, J.G.J. A global high-resolution emission inventory for ammonia. *Global Biogeochem Cy* **1997**, *11*, 561-587.
12. Chen, D.; Yao, X.; Chan, C.K.; Tian, X.; Chu, Y.; Clegg, S.L.; Shen, Y.; Gao, Y.; Gao, H. Competitive uptake of dimethylamine and trimethylamine against ammonia on acidic particles in marine atmospheres. *Environ Sci Technol* **2022**, *56*, 5430-5439.
13. Paulot, F.; Jacob, D.J.; Johnson, M.; Bell, T.G.; Baker, A.R.; Keene, W.C.; Lima, I.D.; Doney, S.C.; Stock, C.A. Global oceanic emission of ammonia: Constraints from seawater and atmospheric observations. *Global Biogeochem Cy* **2015**, *29*, 1165-1178.
14. Song, X.; Basheer, C.; Zare, R.N. Making ammonia from nitrogen and water microdroplets. *Proc. Natl. Acad. Sci.* **2023**, *120*, e1993761176.
15. Zhang, L.; Zhou, Q.; Liang, J.; Yue, L.; Li, T.; Luo, Y.; Liu, Q.; Li, N.; Tang, B.; Gong, F.; Guo, X.; Sun, X. Enhancing electrocatalytic NO reduction to NH3 by the CoS nanosheet with sulfur vacancies. *Inorg Chem* **2022**, *61*, 8096-8102.
16. Liu, Q.; Xu, T.; Luo, Y.; Kong, Q.; Li, T.; Lu, S.; Alshehri, A.A.; Alzahrani, K.A.; Sun, X. Recent advances in strategies for highly selective electrocatalytic N2 reduction toward ambient NH3 synthesis. *Curr Opin Electroche* **2021**, *29*, 100766.
17. Gao, Y.; Yao, X. An adiabatic-expansion-induced perturbation study on gas-aerosol partitioning in ambient air – dimethylamine and trimethylamine (1). *Unpublished Results*.
18. Yu, P.; Hu, Q.; Li, K.; Zhu, Y.; Liu, X.; Gao, H.; Yao, X. Characteristics of dimethylaminium and trimethylaminium in atmospheric particles ranging from supermicron to nanometer sizes over eutrophic marginal seas of China and oligotrophic open oceans. *Sci Total Environ* **2016**, *572*, 813-824.

 doi:10.20944/preprints202503.2201.v1

19. Xie, H.; Feng, L.; Hu, Q.; Zhu, Y.; Gao, H.; Gao, Y.; Yao, X. Concentration and size distribution of water-extracted dimethylaminium and trimethylaminium in atmospheric particles during nine campaigns - Implications for sources, phase states and formation pathways. *Sci Total Environ* **2018**, *631-632*, 130-141.
20. Hu, Q.; Qu, K.; Gao, H.; Cui, Z.; Gao, Y.; Yao, X. Large increases in primary trimethylaminium and secondary dimethylaminium in atmospheric particles associated with cyclonic eddies in the northwest Pacific Ocean. *J. Geophys. Res. Atmos.* **2018**, *123*, 12, 112-133, 146.
21. Shen, Y.; Wang, J.; Gao, Y.; Chan, C.K.; Zhu, Y.; Gao, H.; Petäjä, T.; Yao, X. Sources and formation of nucleation mode particles in remote tropical marine atmospheres over the South China Sea and the Northwest Pacific Ocean. *Sci Total Environ* **2020**, *735*, 139302.
22. Clegg, S.L.; Kleeman, M.J.; Griffin, R.J.; Seinfeld, J.H. Effects of uncertainties in the thermodynamic properties of aerosol components in an air quality model – Part 1: Treatment of inorganic electrolytes and organic compounds in the condensed phase. *Atmos Chem Phys* **2008**, *8*, 1057-1085.
23. Kittelson, D.B. Engines and nanoparticles: a review. *J Aerosol Sci* **1998**, *29*, 575-588.
24. Cass, G.R.; Hughes, L.A.; Bhave, P.; Kleeman, M.J.; Allen, J.O.; Salmon, L.G. The chemical composition of atmospheric ultrafine particles. *Phil. Trans. R. Soc. A.* **2000**, *358*, 2581-2592.
25. Gaffney, J.S.; Marley, N.A. The impacts of peroxyacetyl nitrate in the atmosphere of megacities and large urban areas: a historical perspective. *Acs Earth Space Chem* **2021**, *5*, 1829-1841.
26. Liu, T.; Wang, Y.; Cai, H.; Wang, H.; Zhang, C.; Chen, J.; Dai, Y.; Zhao, W.; Li, J.; Gong, D.; Chen, D.; Zhai, Y.; Zhou, Y.; Liao, T.; Wang, B. Complexities of peroxyacetyl nitrate photochemistry and its control strategies in contrasting environments in the Pearl River Delta region. *Npj Clim Atmos Sci* **2024**, *7*, 116.
27. Heindel, J.P.; LaCour, R.A.; Head-Gordon, T. The role of charge in microdroplet redox chemistry. *Nat Commun* **2024**, *15*, 3670.
28. Yuan, X.; Zhang, D.; Liang, C.; Zhang, X. Spontaneous reduction of transition metal ions by one electron in water microdroplets and the atmospheric implications. *J Am Chem Soc* **2023**, *145*, 2800-2805.
29. Qin, Y.; Wingen, L.M.; Finlayson-Pitts, B.J. Toward a molecular understanding of the surface composition of atmospherically relevant organic particles. *Proc. Natl. Acad. Sci.* **2022**, *119*, e2085833177.
30. Liu, T.; Wang, X.; Wang, B.; Ding, X.; Deng, W.; Lü, S.; Zhang, Y. Emission factor of ammonia (NH3) from on-road vehicles in China: tunnel tests in urban Guangzhou. *Environ Res Lett* **2014**, *9*, 64027.
31. Lee, J.K.; Samanta, D.; Nam, H.G.; Zare, R.N. Micrometer-sized water droplets induce spontaneous reduction. *J Am Chem Soc* **2019**, *141*, 10585-10589.
32. Chen, D.; Shen, Y.; Wang, J.; Gao, Y.; Gao, H.; Yao, X. Mapping gaseous dimethylamine, trimethylamine, ammonia, and their particulate counterparts in marine atmospheres of China's marginal seas – Part 1: Differentiating marine emission from continental transport. *Atmos Chem Phys* **2021**, *21*, 16413-16425.
33. Xiong, H.; Lee, J.K.; Zare, R.N.; Min, W. Strong electric field observed at the interface of aqueous microdroplets. *J. Phys. Chem. Lett.* **2020**, *11*, 7423-7428.